High sensitivity X-ray phase contrast imaging by laboratory grating-based interferometry at high Talbot order geometry

JOAN VILA-COMAMALA,[1,2,*] 🅾 LUCIA ROMANO,[1,2,3] KONSTANTINS JEFIMOVS,[1,2] HECTOR DEJEA,[1,2] ANNE BONNIN,[1,2] ANDREW C. COOK,[4] IVO PLANINC,[5] MAJA CIKES,[5] ZHENTIAN WANG,[1,2] AND MARCO STAMPANONI[1,2]

[1]*Institute for Biomedical Engineering, University and ETH Zürich, 8092 Zürich, Switzerland*
[2]*Paul Scherrer Institut, 5232 Villigen PSI, Switzerland*
[3]*Department of Physics and CNR-IMM, University of Catania, 95023 Catania, Italy*
[4]*University College London Institute of Cardiovascular Science, London WC1E 6BT, United Kingdom*
[5]*Department of Cardiovascular Diseases, University of Zagreb School of Medicine, University Hospital Centre Zagreb, 10000 Zagreb, Croatia*
[*]*joan.vila-comamala@psi.ch*

Abstract: X-ray phase contrast imaging is a powerful analysis technique for materials science and biomedicine. Here, we report on laboratory grating-based X-ray interferometry employing a microfocus X-ray source and a high Talbot order (35th) asymmetric geometry to achieve high angular sensitivity and high spatial resolution X-ray phase contrast imaging in a compact system (total length <1 m). The detection of very small refractive angles (~50 nrad) at an interferometer design energy of 19 keV was enabled by combining small period X-ray gratings (1.0, 1.5 and 3.0 μm) and a single-photon counting X-ray detector (75 μm pixel size). The performance of the X-ray interferometer was fully characterized in terms of angular sensitivity and spatial resolution. Finally, the potential of laboratory X-ray phase contrast for biomedical imaging is demonstrated by obtaining high resolution X-ray phase tomographies of a mouse embryo embedded in solid paraffin and a formalin-fixed full-thickness sample of human left ventricle in water with a spatial resolution of 21.5 μm.

1. Introduction

X-ray imaging [1,2] retrieve information of the sample under investigation by exploiting the absorption, the phase shift or the scattering undergone by the X-ray wavefield traversing the sample material. Employing the phase shift (i.e., the refraction) is particularly suitable for low X-ray absorbing materials such as biological soft tissues, since the refraction interaction is intrinsically two to three orders of magnitude stronger than its absorption counterpart [3]. Because only the intensity of the X-rays can be directly detected, X-ray phase contrast imaging relies on several interference or analyzer methods to transform the phase shifts into measurable intensity modulations in the detector plane [4]. A few examples of these X-ray phase contrast imaging techniques are in-line phase contrast imaging [5,6], grating interferometry [7,8] or analyzer-based imaging [9,10]. These methods were originally developed in synchrotron radiation facilities because they require or profit from the high X-ray flux, the high monochromaticity and the higher spatial coherence delivered by modern synchrotron sources.

X-ray grating interferometry has the particularity that it can be easily realized at conventional laboratory X-ray sources by inserting a source grating, G_0, that relaxes the spatial coherence requirements for the X-ray source [11,12]. Without the necessity of synchrotron radiation, grating-based X-ray phase contrast imaging (gbXPCI) has the potential to be used for a much

wider range of biomedical applications [13–16]. Nevertheless, the performance of laboratory gbXPCI typically encounters several constraints such as the polychromacity of the X-ray photons, the very reduced flux and the source size limiting the achievable spatial resolution. The angular sensitivity [17,18], defined as the smallest refraction angle that can measured, and the spatial resolution are two key defining attributes that need to be optimized in gbXPCI systems. The angular sensitivity can be greatly improved using smaller grating periods or allowing for longer propagation of the X-ray wavefield by increasing the inter-grating distances. For example, the benefits of high angular sensitivity have been recently demonstrated using a long ($\sim$ 1.72 m) laboratory gbXPCI system [18] and employing very small grating periods (200 nm) in synchrotron gbXCPI [13]. On the other hand, the spatial resolution can be improved by using an X-ray tube with a small source size and by taking advantage of the cone beam to obtain a geometrically magnified image of the sample on the detector plane.

   Here, we introduce EXTREME, a tablE-top X-ray phase conTrast micRo computEd toMography systEm which is consists of gbXCPI tool built from state-of-the-art X-ray gratings with periods of 1.0, 1.5 and 3.0 μm in combination with a microfocus X-ray tube delivering a source size of approximately 10 μm. The X-ray gratings have been produced by several microfabrication methods such as deep reactive ion etching of silicon [19], atomic layer deposition of iridium [20] and gold electroplating [21]. Their small periods enable the use of a high Talbot order asymmetric geometry X-ray grating interferometer to achieve high angular sensitivity while substantially shortening the inter-grating distances (total system length $\leq$ 1 m at the X-ray interferometer design energy of 19 keV). Compact interferometer geometries are required when using a microfocus X-ray source, which provides a low divergent X-ray flux at long propagation distances. In addition, a single-photon counting X-ray detector (75 μm pixel size) was employed to reduce the imaging noise as much as possible to Poisson statistics. The overall performance of the interferometer was characterized in terms of angular sensitivity and spatial resolution. Finally, the benefits of the high angular sensitivity provided by our EXTREME system are demonstrated by acquiring X-ray phase tomographies of mouse embryo embedded in solid paraffin and a formalin-fixed full-thickness sample of human left ventricle in water with a spatial resolution of 21.5 μm.

2.   Experimental methods

2.1.   *Grating-based X-ray phase contrast imaging principle*

The X-ray interaction with an object is described by the introduction of a complex refractive index, $n = 1 - \delta + i\beta$, in which the β and δ coefficients respectively account for the absorption and phase shift undergone by the X-ray wavefield due to the specimen. X-ray grating interferometry aims at obtaining the δ coefficient through the measurement of the refractive angle, α. The equation relating the refractive angle α and the δ coefficient is formulated as the following [22],

$$\alpha = \frac{2\pi}{\lambda} \frac{\partial \phi(x,y)}{\partial x} = \frac{\partial}{\partial x} \int_L \delta(x,y,z) dz \qquad (1)$$

where λ is the wavelength of the X-rays, ϕ is the phase of the X-ray wavefield and the line integral is taken along the X-ray wavefield path, L, through the sample.

   In case of laboratory X-ray grating interferometry, typically two highly absorbing gratings, G_0 and G_2, and a phase-shifting grating, G_1, are employed to detect the refractive angle α, as schematically represented in Fig. 1(a). When the right geometry for the X-ray grating periods (p_0, p_1 and p_2) and for the inter-grating distances (l, d) is fulfilled [23], the combination of G_0 and G_1 gratings produce an X-ray intensity modulation downstream of the G_1 grating [8,12]. This interference phenomenon, known as Talbot effect, creates periodic intensity fringes that consists of a nearly identical or geometrically magnified image of the the G_1 grating at certain downstream positions, referred as Talbot distances. The source G_0 grating, enables the use of

an incoherent X-ray source by creating an array of virtual spatial coherent sources that, despite being mutually incoherent, add up constructively when the right geometry is realized [11,23]. On the other hand, a G_2 grating is required to detect the X-ray intensity modulation when the pixel size of the X-ray detector is larger than half the period of the Talbot fringes. For a cone-beam X-ray source, the geometry of the X-ray interferometer is completely determined by the choice of G_1 grating period p_1, the Talbot order m and the Talbot magnification factor M of the Talbot fringes produced by the G_1 grating at the position of G_2 grating [23], so that

$$p_0 = \frac{M}{M-1}\left(\frac{p_1}{\eta}\right), \qquad p_2 = M\left(\frac{p_1}{\eta}\right), \qquad d = MD_m, \qquad l = \frac{M}{M-1}D_m \qquad (2)$$

where the Talbot effect related parameter $\eta = 1$ for a $\pi/2$-shifting phase G_1 grating and $\eta = 2$ for a π-shifting phase G_1 grating. D_m is the fractional Talbot distance of order m produced by the G_1 grating,

$$D_m = \frac{m}{2\lambda}\left(\frac{p_1}{\eta}\right)^2, \quad \text{for} \quad m = 1, 3, 5, \dots \qquad (3)$$

The X-ray intensity modulations are revealed by scanning one of the three gratings in small steps covering a range of one or several grating periods while recording the transmitted intensity, the so-called phase-stepping scan. By taking the maximum and minimum intensities of this recorded oscillating transmission, the visibility [17] is defined as,

$$V = \frac{I_{max} - I_{min}}{I_{max} + I_{min}} \qquad (4)$$

The visibility of a gbXPCI system is an important parameter and has a significant impact on how accurate the refraction angles can be measured. Due to the polychromaticity [17,24] of laboratory sources and the typically limited X-ray absorption of G_0 and G_2 gratings, commonly reported gbXPCI visibilities in laboratory systems range from 10 to 30% [20,25].

When an object is placed near the G_1 phase-shifting grating, the refraction of the X-ray wavefield creates a lateral shift of the Talbot fringes that can be directly related to the refraction angle as follows,

$$\alpha = \frac{p_2}{2\pi d}\varphi \qquad (5)$$

where φ is the X-ray intensity modulation phase shift produced by the sample. This phase shift at every image pixel is measured by two consecutive phase-stepping scans with and without the sample in the X-ray beam path [8]. From Eq. (5), the maximum angular sensitivity has been defined as the smallest refraction angle that can be detected so that [17,18],

$$\alpha_{min} = \frac{p_2}{2\pi d}\sigma_\varphi \qquad (6)$$

in which σ_φ is the standard deviation (noise) of the phase shift φ measurement. For ideal detection conditions with a single-photon counting detector it has been shown that [18,26]

$$\sigma_\varphi = \frac{\sqrt{2}}{V\sqrt{N}} \qquad (7)$$

where V is the visibility of the X-ray grating interferometer and N is the total number of photons of the measurement. From Eqs. (6) and 7, it is worth noticing that the angular sensitivity has a geometrical part that is defined by the choice of the grating period and X-ray interferometer geometry. On the other hand, its second part is related to the total number of photons in the imaging process, mainly determined by the exposure time and X-ray detection efficiency, and the
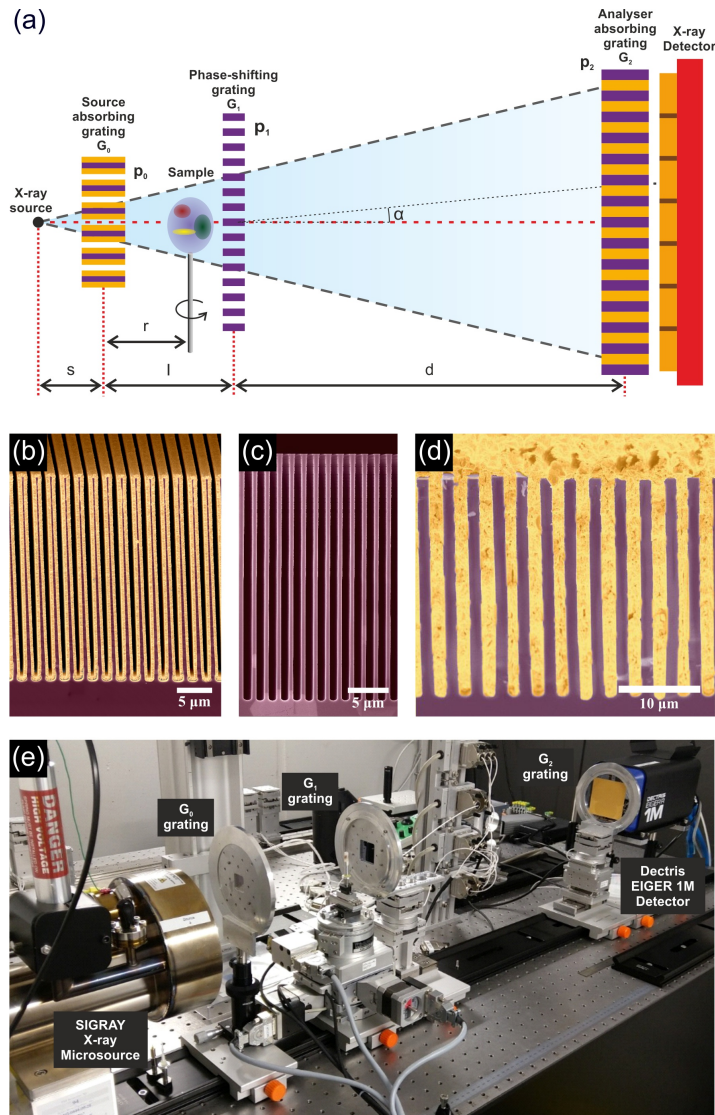
Fig. 1. (a) Schematics of the laboratory grating-based X-ray phase contrast imaging setup composed of two highly absorbing X-ray gratings, G_0 and G_2, and a phase-shifting X-ray grating, G_1. (b) Scanning electron microscopy cross-section of the G_0 grating produced by combining deep reactive ion etching of silicon (purple) and atomic layer deposition of iridium (yellow) (1.0 μm period and 30 μm height). (c) Scanning electron microscopy cross-section of the G_1 grating produced by deep reactive ion etching of silicon (1.5 μm period and 25 μm height). (d) Scanning electron microscopy cross-section of the G_2 grating produced by deep reactive ion etching of silicon (purple) and gold (yellow) electroplating (3 μm period and 35 μm height). (e) Photograph of EXTREME, our laboratory grating-based X-ray phase contrast imaging system.

visibility of the X-ray interferometer, that depends strongly on the X-ray grating quality. Because the sample can not be located exactly at the position of the G_1 grating, the actual refraction angle measurement requires a correction according to following geometric factor [18,27],

$$\alpha_{min} = \frac{l+s}{r+s}\frac{p_2}{2\pi d}\sigma_\varphi \tag{8}$$

where the distance s is the separation between the X-ray source and the G_0 grating and the r is the distance between the G_0 grating and the sample, as displayed in Fig. 1(a). Thus, the closer to the G_1 grating the samples is placed, the smaller refraction angles can be detected [23].

The design of our laboratory gbXCPI system was mainly driven by the intent of using a microfocus X-ray source with a small spot size ($\sim 10~\mu$m) to achieve a spatial resolution well below 50 μm in biological soft tissues. Since X-ray energies ranging from 15 to 25 keV have been demonstrated appropriate for the imaging of biological and biomedical samples [28,29], X-ray energies at around 19 keV were targeted as design parameter of our X-ray interferometer system. From Eq. (6), it explicitly follows that a longer inter-grating distance d and a smaller grating period p_2 will result in the higher angular sensitivity that is required for biological soft tissues. Nevertheless, the choice of the inter-grating distance d and of the G_2 grating period p_2 has to be done according to the Talbot distances for which the Talbot fringes of the G_1 grating occur. Therefore using expressions in Eqs. (2) and 3, one can write that

$$\alpha_{min} = 2\lambda\left(\frac{\eta}{mp_1}\right)\sigma_\varphi \tag{9}$$

This expression clearly shows that the angular sensitivity will in fact decrease (i.e., α_{min} gets larger) due to the use of smaller grating periods unless a high Talbot order geometry is used to compensate for the shortening of the Talbot distances D_m, that scale as the square of p_1 period. Thus, higher angular sensitivity using smaller pitch gratings requires the use of high Talbot order geometry to compensate for the decrease of the propagation distance.

The maximum angular sensitivity α_{min} is a distinctive parameter to evaluate the performance of gbXPCI systems. Details in biological samples have an intrinsically low contrast due to the small refraction angles they produce and will only be visible when gbXPCI system can provide high angular sensitivity to detect such small refractive angles. Taking into account previous published results [18,30] capable of visualizing soft biological tissues, we aimed at an angular sensitivity of at least 50 nrad for our laboratory gbXPCI system. Thus, Table 1 compares four different geometries for X-ray grating interferometer setups targeting at an angular sensitivity better than 50 nrad with a photon energy of 19 keV and considering a imaging noise of $\sigma_\varphi = 0.05$. According to Eq. (7), this value of σ_φ corresponds to an X-ray interferometer with a visibility of $V = 0.15$ and a total number of photons $N \sim 40000$. Such values match well our experimental conditions presented in the sections below. Typically, visibilities between 0.15 and 0.20 were obtained by our X-ray grating interferometer and a total of 40000 photons were involved in the acquisition of the phase-stepping scans. Table 1 shows that reducing the period of the gratings and using high Talbot orders allow to shorten the length of the X-ray interferometer from almost 2 m down to 60 cm while keeping the angular sensitivity at 40 nrad. Here, it is worth noticing that the angular sensitivity does not depend on the Talbot magnification M and as a consequence, different geometries are possible if the right grating periods are chosen. Nevertheless, it can be shown that the minimum length of the X-ray interferometer is $4D_m$ for a Talbot magnification of $M = 2$ [23]. Such configurations are referred as symmetric geometries, in which case $l = d$ and $p_1 = p_2 = p_0$, and they deliver the highest angular sensitivity for a given setup length.

From the X-ray interferometer geometries shown in Table 1, the shortest setup length would be achieved by using a symmetric setup with all grating periods of 1.5 μm. However, another design constraint for our gbXPCI system was the choice of the Dectris EIGER 1M as X-ray detector.

Table 1. Several X-ray grating interferometer geometries to achieve an angular sensitivity of 40 nrad with a design X-ray energy of 19 keV and considering a noise of σ_φ = 0.05 (visibility of V = 0.15 and total number of photons $N \sim 40000$). Small grating periods and high Talbot order geometries are required to shorten the total length, $l + d$, of the X-ray grating interferometer.

	p_1	m	M	p_0	p_2	α_{min}	$l + d$
	[μm]			[μm]	[μm]	[nrad]	[cm]
1	4.8	11	2.0	4.8	4.8	39	192.2
2	3.0	17	2.0	3.0	3.0	40	117.2
3	1.5	35	2.0	1.5	1.5	40	60.3
4	1.5	35	4.0	1.0	3.0	40	80.5

While such single-photon counting detector is very suitable for high efficiency noise-free X-ray detection, that is providing lower values of σ_φ, it has a relatively large pixel size of 75 μm. Because of the high spatial resolution requirements, we decided to use an asymmetric 4× Talbot magnification X-ray interferometer setup so that the effective pixel size in the image was reduced. Due to the non-zero distance between the X-ray source and G_0 grating and because the sample can not be exactly placed at the position of the G_1 grating, the sample image magnification (3.5×) was lower than the Talbot magnification. As a result, the effective image pixel size was 21.5 μm. As displayed in the values for setup 4 of Table 1, the chosen asymmetric X-ray interferometer geometry required a combination of gratings periods of 1.0, 1.5 and 3.0 μm and it used the 35th Talbot order of the G_1 grating. The Talbot magnification of M = 4 slightly elongates the total length of the X-ray grating interferometer but it still remains below 1.0 m, and thus compatible with the low photon flux delivered by the microfocus X-ray source.

2.2. X-ray grating fabrication

The performance of an gbXPCI system crucially relies on availability and quality of the X-ray gratings. In particular, the X-ray absorbing G_0 and G_2 gratings require the fabrication of high aspect ratio metallic structures that completely block the X-ray photons. Typical thicknesses of at least 25–30 μm of a high atomic number element, such as gold, are necessary to stop X-ray energies of around 20 keV. To date, the microfabrication methods to produce highly absorbing X-ray gratings combine optical or X-ray lithography with gold electroplating in silicon [19,31] or polymer resist [32] molds. However, such techniques are not easily transferred to the fabrication of sub-micrometer high aspect ratio structures such as X-ray absorbing gratings with periods below 2.0 μm.

The required gratings were produced in-house using 4-inch double side polished silicon wafers with a thickness of 250 μm, that is, a sufficiently thin supporting substrate to minimize the absorption at X-ray energies of around 20 keV. The G_0 grating with a period of 1.0 μm and a thickness of 30 μm used in our gbXPCI system was produced by combining optical lithography, deep reactive ion etching of silicon [19] and atomic layer deposition of iridium [20]. First, the silicon wafer was patterned with optical lithography with a period 2.0 μm but the grating trenches were on purpose made wider so that after a conformal deposition of iridium the periodicity of the grating was doubled to achieve an aspect ratio of 60 for the 1.0 μm period structures. The patterned area had a total size of 2 × 2 cm^2, which was large enough to employ the grating as G_0. Such a zone-doubling method has been already successfully used for the fabrication of high resolution X-ray diffractive optics [33]. A scanning electron micrograph of the 1.0 μm period structures is shown in Fig. 1(b), in which false colors have been added to clearly distinguish between the iridium layer (yellow) and the silicon template (purple). More extensive details of the fabrication process of this X-ray gratings have been published elsewhere [20]. The G_1 grating pattern with 1.5 μm period was exposed by electron beam lithography and then transferred by

deep reactive ion etching into the silicon wafer substrate. The exposed area was approximately 2×2 cm^2 and the depth of the etched grating trenches was 25 μm, a value that was selected to deliver a π phase shift for an X-ray energy of 20 keV. Figure 1(c) displays a scanning electron micrographs of the cross-section of the G_1 grating. On the other hand, the X-ray absorbing G_2 grating was produced on a 4-inch silicon wafer with a patterned area size of 7×7 cm^2 by standard photolithography. The exposed grating pattern had a period of 3.0 μm and both the photolithography and the deep silicon reactive ion etching were optimized to obtain 30 to 35 μm deep trenches. The gaps were then filled with gold by seedless conformal electroplating process using low resistivity silicon wafer [21,31]. A scanning electron microscopy image of the cross-section of the G_2 grating is exhibited in Fig. 1(d), in which false colors have been used to clearly distinguish between the gold (yellow) and the silicon (purple).

2.3. Implementation of the laboratory grating-based X-ray phase contrast imaging

Our gbXPCI setup was composed of a microfocus X-ray source with a tungsten target (Sigray Inc) and an expected X-ray source size of approximately 10 μm. The microfocus X-ray source was operated at a voltage of 40 kV and electron beam currents up to 1.5 mA. The Dectris EIGER 1M detector had a silicon sensor thickness of 450 μm and a total of 1030×1065 pixels of 75 μm. The quantum efficiency of such detector is about 40% at the design energy of the interferometer. Despite this value is not optimum, the Dectris EIGER 1M detector was performing much better than other flatpanel detectors that were tested during the preparation of the setup both in terms of spatial resolution and detection efficiency. The gratings were mounted on motorized stages (SmarAct GmbH) with 20 nm position accuracy for alignment and phase-stepping scan acquisitions. The stages allowed adjustment of all angles of the G_1 and G_2 gratings. As mentioned above, the X-ray interferometer geometry was chosen according to specifications of setup 4 in Table 1, combining grating periods of 1.0, 1.5 and 3.0 μm. The samples were mounted on a motorized stage (HUBER Diffraktionstechnik GmbH) allowing accurate sample rotation during the tomographic acquisitions. In addition to the rotation required for tomography, the sample stage allowed the tilt adjustments for a precise alignment of the rotation axis before the tomography acquisitions.

During the assembly of the system, the X-ray gratings were carefully aligned until the typical Morié fringes disappeared completely. We chose the distance s between the X-ray source and the G_0 grating to be 10 cm. The distance between the G_0 grating and the sample was $r = 16.5$ cm and the inter-grating distances were $l = 20.1$ cm and $d = 60.3$ cm, corresponding to the 35th Talbot order of the G_1 grating for a design X-ray energy of 19 keV, as previously explained. A picture of our laboratory gbXPCI system is shown in Fig. 1(e). Typical exposure times per phase-stepping scan position range from 5 s during the alignment procedure to up to 50 s during the acquisition of the X-ray phase tomography data. Longer exposure times could be used to obtain higher angular sensitivity, but then the total acquisition time for tomography scans would be impracticable and effects of mechanical instabilities might appear. The G_2 grating with the largest period of 3.0 μm was the one moved during the acquisition of the phase-stepping scans so that any positioning inaccuracies would have the lowest repercussion in the recorded data. The phase-stepping scans of 5 grating positions were typically used to retrieve the X-ray phase information. As expected, the choice of the asymmetric 4× Talbot magnification X-ray interferometer delivered the highest angular sensitivity with high spatial resolution while relaxing the requirement on X-ray grating specifications.

3. Results and discussion

3.1. *Angular sensitivity characterization of the X-ray grating interferometer*

After assembling and aligning our gbXPCI according to the above described asymmetric 4×
Talbot magnification geometry, the system was characterized using a test sample consisting of
polystyrene microspheres with a diameter of 700 μm. Figures 2(a) and (b) shows the visibility at
every pixel and the visibility histogram of the usable field of view of our X-ray phase contrast
imaging system. The peak value of the visibility histogram was at 19.5%, which confirms the
good quality of the X-ray gratings despite their small periods. The visibility at every pixel was
calculated from the phase-stepping scan intensity images by the commonly used Fourier analysis
[7,34]. Such method delivers more reliable visibility values than directly applying Eq. (4) when
only a small number of the phase-stepping scan points are used. At the edges of the field of view
the visibility decreases due to the mismatch of a flat G_0 grating and the cone-beam produced by
our microfocus X-ray source. Nevertheless, the usable field of view is about 1.3×1.7 cm^2 and it
could be enlarged in the future by the use of bendable gratings. The black horizontal gap at the
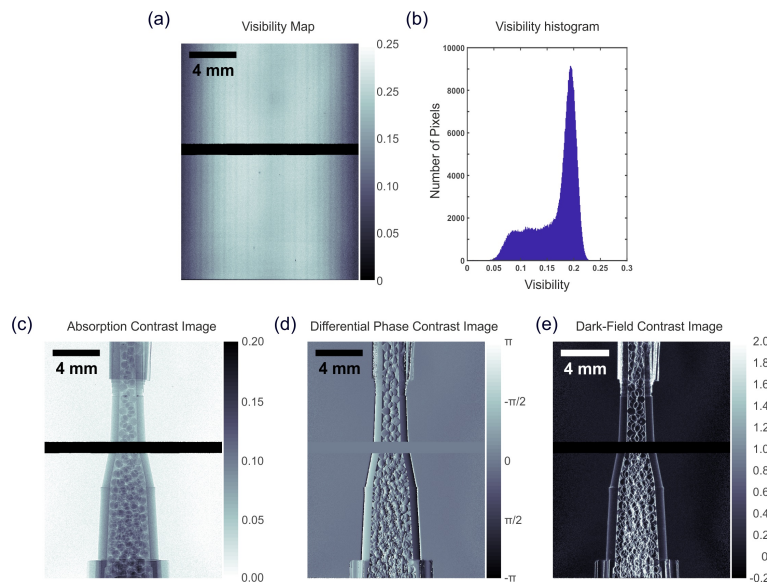center of the images is due to non-sensitive area of the Dectris EIGER 1M detector.

Fig. 2. (a) Visibility map, that is at every pixel, of the implemented grating-based X-ray
phase contrast imaging system. The visibility is reduced at the edge of field of view due to
the mismatch of flat grating with the cone-beam delivered by the source. (b) Histogram of
the visibility with a peak value of 0.195. (c) Absorption and (d) differential phase contrast
images of polystyrene microspheres of 700 μm. After calculating the standard deviation in
the empty space of the differential phase contrast image, the angular sensitivity is estimated
to be 45 nrad. (e) Dark-field contrast image of the polystyrene microspheres. The stripe
across the images is due to the dead zone of the Dectris EIGER 1M detector.

Figures 2(c), (d) and (f) exhibit the absorption, the differential phase contrast and dark-field
images of the polystyrene spheres in a plastic container, also calculated using the Fourier analysis
[7,34] of phase-stepping scans. The absorption image is substantially noisier than the differential
phase image due to the low absorption of the polystyrene spheres. The standard deviation of
an empty area of the differential phase contrast image (100×100 pixels) was measured to be
$\sigma_\varphi = 0.051$. Thus, using Eq. (8) we can estimate an angular sensitivity of 45 nrad. To date,

such a high angular sensitivity values have been only been reported using a longer ($\sim$ 1.72 m) laboratory gbXPCI that combines an X-ray source with a spot size of 100 μm (much higher photon flux than for a microfocus X-ray source) and an X-ray detector with much larger pixel 172 μm [18].

In addition, we also investigated the angular sensitivity as function of the X-ray source parameters. Figure 3(a) shows the variation of angular sensitivity as function of the electron beam current at a constant acceleration voltage of 40 kV. Complementary, Fig. 3(b) shows the variation of the angular sensitivity as function of the electron acceleration voltage at constant electron beam current of 1.5 mA. In both cases, the sensitivity is shown for several exposure times per frame (5 phase-stepping scan positions were used). On the one hand, the angular sensitivity increases with the electron beam current because more X-ray photons are generated. On the other hand, the increase of the source electron acceleration voltage does not produce a significant change in the angular sensitivity. This is most likely explained because the electron acceleration voltage increment preferentially boosts the generation of high X-ray energy photons for which the absorbing X-ray gratings are more transparent and thus reducing the visibility of the X-ray interferometer. From these measurements, we fixed the working parameters of our X-ray source to a voltage of 40 kV and electron current of 1.5 mA.

Moreover, using an X-123 CdTe X-ray spectrometer (Amptek Inc.), we acquired a phase-stepping scan to investigate the visibility as function of the X-ray energy shown in Fig. 3(c). For this measurement, the X-ray spectrometer was placed right behind the central area of G_2 grating after aligning the X-ray interferometer. Then, the energy spectrum transmitted through the X-ray interferometer was measured at every position of the phase-stepping scan for a time of 300 s. Finally, the Fourier analysis of the phase-stepping scan was applied for every energy acquisition channel of the X-ray spectrometer. Using a high Talbot order geometry, there exist many visibility peaks that can be paired to different X-ray energies corresponding to a different Talbot orders. Table 2 shows that the X-ray energies of every visibility peak can be indeed matched with the X-ray energies calculated from Eqs. (2) and 3 and they correspond to higher and lower Talbot orders for which the required geometry of the X-ray interferometer is exactly the same. From this graph, we also observe that after the alignment of the gratings, the 35th Talbot order corresponded to an actual X-ray energy of 18.76 keV.

Table 2. The visibility peaks as function of the X-ray energy, shown in Fig. 3(c), can be matched to calculated X-ray energies that fulfill the geometry of the X-ray interferometer for different Talbot orders.

Measured Energy [keV]	m	Calculated Energy [keV]
16.74	39	16.85
17.71	37	17.76
18.76	35	-
19.92	33	19.92
21.31	31	21.20
22.73	29	22.67
24.65	27	24.35

3.2. *Calibration of the X-ray grating interferometer*

Further characterization of our laboratory gbXPCI system was done by acquiring a tomography of a sample containing several known organic liquids. The container was placed on the rotation stage in air. After obtaining the differential phase contrast image at every projection angle, it is possible to retrieve the δ coefficient of the refractive index during the tomographic reconstruction
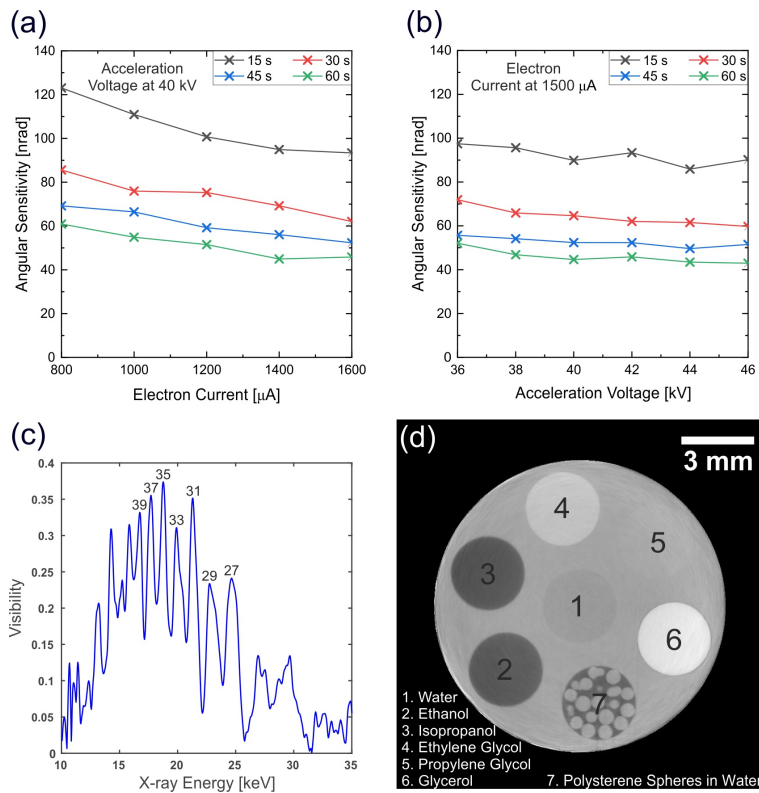
Fig. 3. (a) Variation of the angular sensitivity for our gbXPCI system as function of electron beam current of the microfocus X-ray source and for different acquisition times per phase-stepping scan position. (b) Variation of the angular sensitivity for our gbXPCI as function of acceleration voltage of the microfocus X-ray source and for different acquisition times per phase-stepping scan position. (c) Measured visibility as function of X-ray energy spectrum. Several peaks of the visibility curve can be matched to lower and higher Talbot order corresponding to different X-ray energy. (d) Slice of tomographic reconstruction containing several know organic liquids that can be used as a calibration sample for the laboratory gbXPCI.

by replacing the commonly used Ram-Lak filter by Hilbert filter, as has been shown in the past [35–37]. A total of 721 differential phase contrast projections covering an angle range from 0 to 180 deg were recorded. The phase wrapping at the edges of the container was manually corrected by adding or subtracting the required multiple of 2π. The fan-beam geometry of the ASTRA tomographic reconstruction toolbox [38] was used for this calibration sample. From the reconstructed slice presented in Fig. 3(d), we compared the measured δ coefficient of water to its theoretically expected value [39] and we determined an effective X-ray energy of our gbXPCI setup to be 24.8 keV. After that, the tabulated δ coefficient of the other organic liquids at 24.8 keV [39] could be well matched with the experimentally obtained δ coefficients. The comparison of the measured and expected values of the refractive index δ coefficients for each liquid are listed in Table 3. The mismatch between the design X-ray energy and the measured effective X-ray energy is likely to be a result of the high Talbot geometry and the spectrum of X-ray energies reaching the detector. It will be further investigated in future works. Nevertheless, the phase measurements can be made quantitative because the X-ray interferometer system can be calibrated with known substances and the measured and calculated values of δ are consistent. In Table 3 one can see that small variations down to 10^{-8} of the δ coefficient could be successfully measured. The error of the measured δ coefficients was derived from the standard deviation of measured value in an area inside the liquid volume. In future works, known biological materials could be used for the calibration and for obtaining the electron density of biological tissues [29,40].

Table 3. The grating-based X-ray phase contrast imaging system can be calibrated using a given liquid (water) and matching the retrieved δ coefficient with its theoretically expected value. After that, the tabulated δ coefficients of the other organic liquids at the determined X-ray energy matched well the experimentally measured values.

	Liquid	Formula	Density [g/cm^3]	$\delta_{measured}[10^{-6}]$	$\delta_{theoretical}[10^{-6}]$
1	Water	H_2O	1.0000	0.384 ± 0.002	-
2	Ethanol	C_2H_6O	0.7893	0.306 ± 0.003	0.308
3	Isopropanol	C_3H_8O	0.7860	0.311 ± 0.004	0.308
4	Ethylene Glycol	$C_2H_6O_2$	1.1132	0.428 ± 0.002	0.421
5	Propylene Glycol	$C_3H_8O_2$	1.0360	0.398 ± 0.002	0.396
6	Glycerol	$C_3H_8O_3$	1.2610	0.463 ± 0.003	0.473
	Container	-	-	0.391 ± 0.002	-

3.3. Spatial resolution characterization and phase contrast X-ray imaging of biological soft tissues

The performance of our gbXPCI was also evaluated by obtaining phase contrast X-ray tomographies of two biological soft tissue samples. The first sample was a mouse embryo embedded in solid paraffin of an approximate size of $4 \times 4 \times 8$ mm^3. Animal maintenance, husbandry and procedures were done in accordance with British Home Office regulations (Animals Scientific Procedures Act 1986). The mouse embryo was fixed in 4% paraformaldehyde (PFA) in phosphate buffered saline (PBS) for 12 hours. Then, it was dehydrated by increasing an ethanol concentration from 30% to 100%. After that, it was cleared using histoclear (National Diagnostics) for one hour, and embedded in paraffin for 12 hours after several wax washes at 60 deg C. Finally, the paraffin block was cut down to a small cylinder around the mouse embryo. The sample was then mounted on the rotation stage and a total of 601 differential phase contrast projections were acquired at angles ranging from 0 to 180 deg. Each projection was acquired with a 5 position phase-stepping scan with an acquisition of 50 s per frame. Reference phase-stepping scans without sample were taken regularly every 10 projections, to compensate for any position drifts of the gratings or any movements of X-ray source spot. The total acquisition time was about 45

hours. The tomographic reconstruction was obtained using the filtered-back projection routine from the ASTRA tomographic reconstruction toolbox [38]. As described in the previous section, the standard Ram-Lak filter was substituted by Hilbert filter to directly retrieve the phase signal from acquired differential phase images [35–37]. In this case, the cone-beam geometry available in the ASTRA toolbox was used. The parameters of the reconstruction were taken from the setup geometry and slightly adjusted until the optimal reconstruction was obtained. Figure 4 shows several sagittal slices through the tomographic reconstruction in which the internal organs and bone structure of the mouse embryo can be observed and clearly identified. A few of these have been labeled in Fig. 4. It is worth noticing, that the biological material was just dried and embedded in paraffin but no staining was applied [41]. This opens up the investigation of biological material by X-ray computer tomography in conditions closer to its natural state.
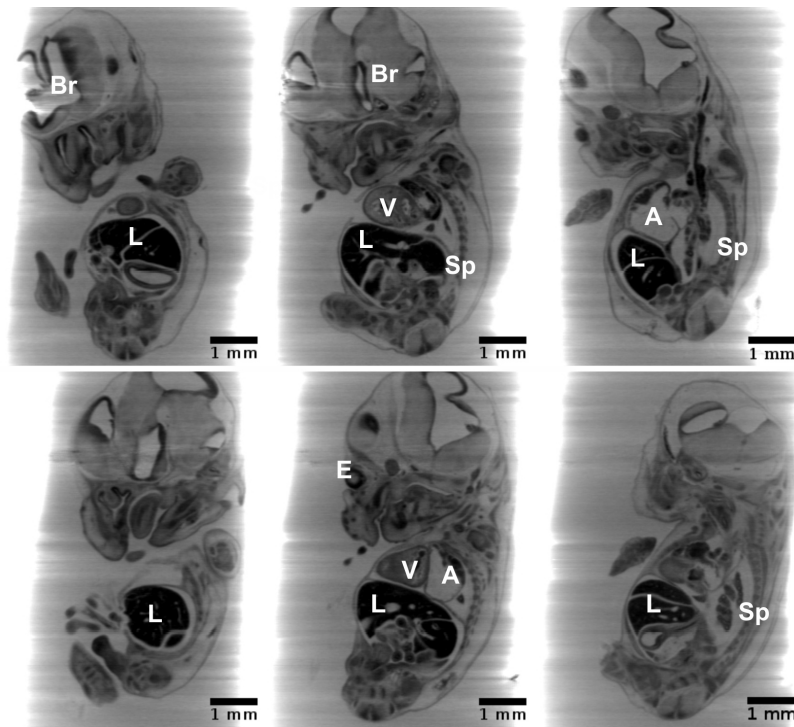

Fig. 4. X-ray phase tomographic reconstruction slices of a mouse embryo embedded in solid paraffin. A total of 601 differential phase contrast projections using phase-stepping scans of 5 positions were collected covering a rotation angle from 0 to 180 deg. The internal organs and bone structure are clearly visible and can be identified. Labeling: Br–Brain; L–Liver; V–Ventricle; A–Atrium; E–Eye; Sp–Spine.

A second tomographic reconstruction of the mouse embryo with the exact same parameters was acquired to determine the spatial resolution achieved in our system. We applied the Fourier ring correlation analysis [42,43] to determine the spatial resolution of the images using two identical but independently acquired tomographic reconstruction slices. Figure 5 shows the Fourier ring correlation curve from the processing of the two slices of the mouse embryo reconstructions compared to the 1-bit threshold curve [42,43]. Because the Fourier ring correlation curve does not cut the 1-bit threshold curve, we can estimate the spatial resolution of mouse embryo tomographic slices to be the effective pixel size of 21.5 μm. Thus in our current configuration, the spatial resolution is limited by the detector pixel size but not constrained by the source size of

our microfocus X-ray tube. This is consistent with the estimated X-ray source size of 10 to 15 μm, and higher spatial resolution could be achieved by using an X-ray detector with a smaller pixel size. To date, laboratory gbXCPI with high angular sensitivity [18] could only demonstrate a spatial resolution down to 100 μm due to the use of X-ray source with a much larger spot size. In future works, the use of recently reported super-resolution techniques [44–46] could further increase the spatial resolution of our phase contrast imaging system.
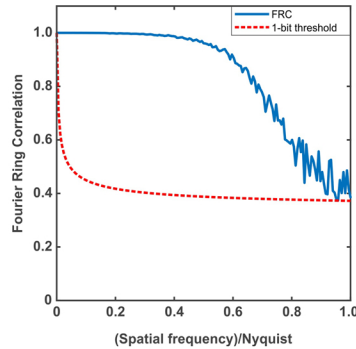

Fig. 5. Fourier ring correlation curve calculated from two identical but independently acquire X-ray phase tomographic slices of the mouse embryo. Because the Fourier ring correlation curve does not cut the 1-bit threshold curve, we can estimate the spatial resolution to be as good at the effective pixel size of 21.5 μm.

The second tomographic acquisition was done on a formalin-fixed full-thickness sample of a human ventricle preserved in buffered formalin solution with an approximate sample size of $5 \times 7 \times 8$ mm^3. The tissue was harvested from the explanted heart of a patient undergoing heart transplantation due to advanced heart failure caused by severe ischemic heart disease. The patient signed informed consent, and the ethical approval was obtained for the study (Ethics Committee of the University Hospital Centre Zagreb approval; Class: 8.1-17/137-2; Number: 02/21 AG). Prior to the tomographic acquisition, the sample was placed in a container and the liquid formalin was replaced by degassed water [47]. A total of 721 differential phase contrast projections were acquired from angles ranging from 0 to 180 deg. Each projection was acquired with a phase-stepping scan of 5 positions and an acquisition time of 50 s per frame. Again, reference phase-stepping scans were taken regularly every 10 projections and the total acquisition time was about 60 hours. Figure 6 depicts six representative tomographic slices of the human full-thickness heart sample. The angular sensitivity and the spatial resolution of the laboratory gbXPCI system allows to visualize different integral parts of cardiac full-thickness sample. We assume that the brightest (white) areas correspond to non-contractile parts of the heart muscle, such as fibrous and fatty structural elements. Grey areas indicate contractile part of the heart muscle, i.e. myocardium. Furthermore, the acquired images allow discrimination between compacted and non-compacted parts of the heart muscle, such that the non-compacted parts indicate the localization of endocardium. The different types of tissue has been labeled in Fig. 6.
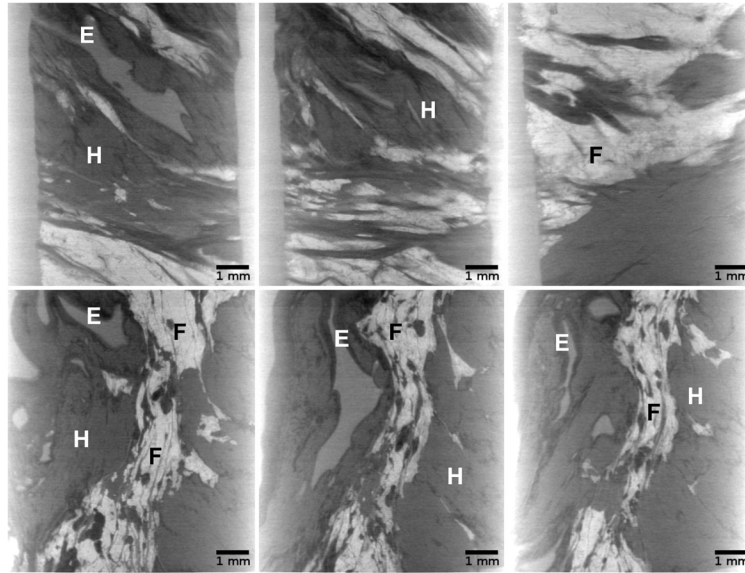
Fig. 6. X-ray phase tomographic reconstruction slices of formalin-fixed full-thickness sample of a human left ventricle. The specimen was placed in a container with degassed water prior to the tomographic scan. A total of 721 differential phase contrast projections using phase-stepping scans of 5 positions were collected covering a rotation angle from 0 to 180 deg. Fibrous and fatty structural elements (brightest/ white areas), and contractile parts of the heart muscle (grey areas) can be observed. The non-compacted areas indicate the localization of endocardium. Labeling: E–Endocardium-endothelial lining of the heart; F–Fibrous and fatty structural elements; H–Heart muscle- contractile part of the heart wall.

4. Conclusions

We have demonstrated the use of a laboratory asymmetric high Talbot order grating-based X-ray interferometer for achieving X-ray phase contrast imaging of biological soft tissues with high angular sensitivity ($\sim$ 45 nrad) and high spatial resolution ($\sim$ 21.5 μm). This performance was enabled by the combination of small grating periods down to 1.0 μm, a laboratory microfocus X-ray source and single-photon counting detector. The recently developed fabrication method combining silicon reactive ion etching and atomic layer deposition paves the way for the production of high aspect ratio X-ray absorbing gratings with period below 1.0 μm for X-ray interferometry. In this work, the use of small period gratings was essential to reduce the total interferometer length to about 80 cm, thus making the setup functional while using the very low photon flux delivered by the microfocus X-ray source. In addition, the asymmetric high Talbot order X-ray interferometer geometry provided the high angular sensitivity necessary to visualize the soft biological material. The geometric magnification ($\sim$ 3.5$\times$) of the system made the use of a large detector pixel size (75μm) compatible with achieving an effective pixel size and spatial resolution of 21.5 μm. Two X-ray phase tomograms of biological soft tissues have been successfully obtained and they show the potential of laboratory X-ray grating interferometry for improving pathology and medical diagnosis in the future.

Disclosures. The authors declare no conflicts of interest.

References

1. S. R. Stock, "Recent advances in x-ray microtomography applied to materials," Int. Mater. Rev. **53**(3), 129–181 (2008).
2. E. Maire and P. J. Withers, "Quantitative x-ray tomography," Int. Mater. Rev. **59**(1), 1–43 (2014).
3. D. Attwood, *Soft X-rays and Extreme Ultraviolet Radiation* (Cambridge University, 2000).
4. J. Als-Nielsen and D. McMorrow, *Elements of Modern X-ray Physics, Second Edition* (John Wiley & Sons, 2010).
5. P. Cloetens, W. Ludwig, J. Baruchel, D. V. Dyck, J. V. Landuyt, J. P. Guigay, and M. Schlenker, "Holotomography: Quantitative phase tomography with micrometer resolution using hard synchrotron radiation x-rays," Appl. Phys. Lett. **75**(19), 2912–2914 (1999).
6. K. A. Nugent, T. E. Gureyev, D. F. Cookson, D. Paganin, and Z. Barnea, "Quantitative phase imaging using hard hard x-rays," Phys. Rev. Lett. **77**(14), 2961–2964 (1996).
7. A. Momose, S. Kawamoto, I. Kowama, Y. Hamaishi, K. Takai, and Y. Suzuki, "Demonstration of x-ray talbot interferometry," Jpn. J. Appl. Phys. **42**(Part 2, No. 7B), L866–L868 (2003).
8. T. Weitkamp, A. Diaz, C. David, F. Pfeiffer, M. Stampanoni, P. Cloetens, and E. Ziegler, "X-ray phase imaging with a grating interferometer," Opt. Express **13**(16), 6296 (2005).
9. V. N. Ingal and E. A. Beliaevskaya, "X-ray plane-wave topography observation of phase contrast from a non-crystalline object," J. Phys. D: Appl. Phys. **28**(11), 2314–2317 (1995).
10. D. Chapman, W. Thomlinson, R. E. Johnston, D. Wahsburn, E. Pisano, N. Gmür, Z. Zhong, R. H. Menk, F. Felli, and D. Sayers, "Diffraction enhanced x-ray imaging," Phys. Med. Biol. **42**(11), 2015–2025 (1997).
11. F. Pfeiffer, T. Weitkamp, O. Bunk, and C. David, "Phase retrieval and differential phase-contrast imaging with low-brilliance x-ray sources," Nat. Phys. **2**(4), 258–261 (2006).
12. M. Engelhardt, J. Baumann, M. Schuster, C. Kottler, F. Pfeiffer, O. Bunk, and C. David, "High-resolution differential phase contrast imaging using a magnifying geometry with a microfocus x-ray source," Appl. Phys. Lett. **90**(22), 224101 (2007).
13. H. Wen, A. A. Gomella, A. Patel, S. K. Lynch, N. Y. Morgan, S. A. Anderson, E. E. Bennett, X. Xiao, C. Liu, and D. E. Wolfe, "Subnanoradian x-ray phase-contrast imaging using a far-field interferometer of nanometric phase gratings," Nat. Commun. **4**(1), 2659 (2013).
14. Z. Wang, N. Hauser, G. Singer, M. Trippel, R. Kubik-Huch, C. Schneider, and M. Stampanoni, "Non-invasive classification of microcalcifications with phase-contrast x-ray mammography," Nat. Commun. **5**(1), 3797 (2014).
15. C. Arboleda, Z. Wang, T. Koehler, G. Martens, U. V. Stevendaal, M. Bartels, P. Villanueva-Perez, E. Roessl, and M. Stampanoni, "Sensitivity-based optimization for the design of a grating interferometer for clinical x-ray phase contrast mammography," Opt. Express **25**(6), 6349–6364 (2017).
16. L. B. Gromann, F. De Marco, K. Willer, P. B. Noël, K. Scherer, B. Renger, B. Gleich, K. Achterhold, A. A. Fingerle, D. Muenzel, S. Auweter, K. Hellbach, M. Reiser, A. Baehr, M. Dmochewitz, T. J. Schroeter, F. J. Koch, P. Meyer, D. Kunka, J. Mohr, A. Yaroshenko, H.-I. Maack, T. Pralow, H. van der Heijden, R. Proksa, T. Koehler, N. Wieberneit, K. Rindt, E. J. Rummeny, F. Pfeiffer, and J. Herzen, "In-vivo X-ray Dark-Field Chest Radiography of a Pig," Sci. Rep. **7**(1), 4807 (2017).
17. T. Thuering and M. Stampanoni, "Performance and optimization of x-ray grating interferometry," Philos. Trans. R. Soc. A **372**(2010), 20130027 (2014).
18. L. Birnbacher, M. Willner, A. Velroyen, M. Marschner, A. Hipp, J. Meiser, K. Frieder, T. Schöter, D. Kunka, J. Mohr, F. Pfeiffer, and J. Herzen, "Experimental realisation of high-sensitivity laboratory x-ray grating-based phase-contrast computed tomography," Sci. Rep. **6**(1), 24022 (2016).
19. K. Jefimovs, L. Romano, J. Vila-Comamala, M. Kagias, Z. Wang, L. Wang, C. Dais, H. Solak, and M. Stampanoni, "High aspect ratio silicon structures by displacement talbot lithography and bosch etching," Proc. SPIE **10146**, 101460L (2017).
20. J. Vila-Comamala, L. Romano, V. Guzenko, M. Kagias, M. Stampanoni, and K. Jefimovs, "Towards sub-micrometer high aspect ratio x-ray gratings by atomic layer deposition of iridium," Microelectron. Eng. **192**, 19–24 (2018).
21. M. Kagias, Z. Wang, V. A. Guzenko, C. D. M. Stampanoni, and K. Jefimovs, "Fabrication of au gratings by seedless electroplating for x-ray grating interferometry," Mater. Sci. Semicond. Process. **92**, 73–79 (2019).
22. D. M. Paganin, *Coherent X-ray Optics* (Oxford University, 2006).
23. T. Donath, M. Chabior, F. Pfeiffer, O. Bunk, E. Reznikova, J. Mohr, E. Hempel, S. Popescu, M. Hoheisel, M. Schuster, B. Joachim, and C. David, "Inverse geometry for grating-based x-ray phase-contrast imaging," J. Appl. Phys. **106**(5), 054703 (2009).
24. A. Hipp, M. Willner, J. Herzen, S. Auweter, M. Chabior, J. Meiser, K. Achterhold, J. Mohr, and F. Pfeiffer, "Energy-resolved visibility analysis of grating interferometers operated at polychromatic x-ray sources," Opt. Express **22**(25), 30394–30409 (2014).
25. L. Romano, J. Vila-Comamala, K. Jefimovs, and M. Stampanoni, "High-aspect-ratio grating microfabrication by platinum-assisted chemical etching and gold electroplating," Adv. Eng. Mater. **22**(10), 2000258 (2020).
26. R. Raupach and T. G. Flohr, "Analytical evaluation of the signal and noise propagation in x-ray phase contrast computed tomography," Phys. Med. Biol. **56**(7), 2219–2244 (2011).

27. J. Herzen, T. Donath, F. Pfeiffer, O. Bunk, C. Padeste, F. Beckmann, A. Schreyer, and C. David, "Quantitative phase-contrast tomography of a liquid phantom using a conventional x-ray tube source," Opt. Express **17**(12), 10010–10018 (2009).

28. S. A. McDonald, F. Marone, C. Hintermüller, G. Mikuljan, C. David, F. Pfeiffer, and M. Stampanoni, "Advanced phase-contrast imaging using a grating interferometer," J. Synchrotron Rad. **16**(4), 562–572 (2009).

29. M.-C. Zdora, J. Vila-Comamala, G. Schulz, A. Khimchenko, A. Hipp, A. C. Cook, D. Dilg, C. David, C. Grünzweig, C. Rau, P. Thibault, and I. Zanette, "X-ray phase microtomography with a single grating for high-throughput investigations of biological tissue," Biomed. Opt. Express **8**(2), 1257–1270 (2017).

30. P. Modregger, B. R. Pinzer, T. Thüring, S. Rutishauser, C. David, and M. Stampanoni, "Sensitivity of x-ray grating interferometry," Opt. Express **19**(19), 18324–18338 (2011).

31. K. Jefimovs, J. Vila-Comamala, C. Arboleda, L. Romano, Z. Shi, M. Kagias, and M. Stampanoni, "Fabrication of x-ray gratings for interferometric imaging by conformal seedless gold electroplating," Submitted (2021).

32. J. Mohr, T. Grund, D. Kunka, J. Kenntner, J. Leuthold, J. Meiser, J. Schulz, and M. Walter, "High aspect ratio gratings for x-ray phase contrast imaging," AIP Conf. Proc. **1466**, 41–50 (2012).

33. K. Jefimovs, J. Vila-Comamala, T. Pilvi, J. Raabe, M. Ritala, and C. David, "Zone-doubling technique to produce ultrahigh-resolution x-ray optics," Phys. Rev. Lett. **99**(26), 264801 (2007).

34. S. Kaeppler, J. Rieger, G. Pelzer, F. Horn, T. Michel, A. Maier, G. Anton, and C. Riess, "Improved reconstruction of phase-stepping data for talbot–lau x-ray imaging," J. Med. Imag. **4**(03), 1 (2017).

35. Z. Huang, K. Kang, Z. Li, P. Zhu, Q. Yuan, W. Huang, J. Wang, D. Zhang, and A. Yu, "Direct computed tomographic reconstruction for directional-derivativeprojections of computed tomography of diffraction enhanced imaging," Appl. Phys. Lett. **89**(4), 041124 (2006).

36. F. Pfeiffer, C. Kottler, O. Bunk, and C. David, "Hard x-ray phase tomography with low-brilliance sources," Phys. Rev. Lett. **98**(10), 108105 (2007).

37. D. Pelliccia, R. Vaz, I. Svalbe, K. S. Morgan, S. Marathe, X. Xiao, L. Assoufid, R. A. Anderson, J. Topczewski, and R. J. Bryson-Richardson, "Comparison of different numerical treatments for x-ray phase tomography of soft tissue from differential phase projections," Phys. Med. Biol. **60**(8), 3065–3080 (2015).

38. W. van Aarle, W. J. Palenstijn, J. Cant, E. Janssens, F. Bleichrodt, A. Dabravolski, J. D. Beenhouwer, K. J. Batenburg, and J. Sijbers, "Fast and flexible x-ray tomography using the astra toolbox," Opt. Express **24**(22), 25129–25147 (2016).

39. "The Center for X-ray Optics, X-ray interactions with matter," https://henke.lbl.gov/optical_constants/.

40. R. Gradl, I. Zanette, M. Ruiz-Yaniz, M. Dierolf, A. Rack, P. Zaslansky, and F. Pfeiffer, "Mass density measurement of mineralized tissue with grating-based x-ray phase tomography," PLoS One **11**(12), e0167797 (2016).

41. C. Hsu, S. Kalaga, U. Akoma, T. L. Rasmussen, and A. E. C. M. E. Dickinson, "High resolution imaging of mouse embryos and neonates with x-ray micro-computed tomography," Curr. Protoc. Mouse Biol. **9**(2), e63 (2019).

42. M. van Heel and M. Schatz, "Fourier shell correlation threshold criteria," J. Struct. Biol. **151**(3), 250–262 (2005).

43. J. Vila-Comamala, S. Gorelick, E. Farm, C. M. Kewish, A. Diaz, R. Barrett, V. A. Guzenko, M. Ritala, and C. David, "Ultra-high resolution zone-doubled diffractive x-ray optics for the multi-kev regime," Opt. Express **19**(1), 175–184 (2011).

44. M. Viermetz, L. Birnbacher, M. Willner, K. Achterhold, F. Pfeiffer, and J. Herzen, "High resolution laboratory grating-based x-ray phase-contrast ct," Sci. Rep. **8**(1), 15884 (2018).

45. K. R. Rix, T. Dreier, T. Shen, and M. Bech, "Super-resolution x-ray phase-contrast and dark-field imaging with a single 2d grating and electromagnetic source stepping," Phys. Med. Biol. **64**(16), 165009 (2019).

46. T. Dreier, U. Lundström, and M. Bech, "Super-resolution x-ray imaging with hybrid pixel detectors using electromagnetic source stepping," J. Instrum. **15**(03), C03002 (2020).

47. H. Dejea, P. Garcia-Canadilla, A. C. Cook, E. Guasch, M. Zamora, F. Crispi, M. Stampanoni, B. Bijnens, and A. Bonnin, "Comprehensive analysis of animal models of cardiovascular disease using multiscale x-ray phase contrast tomography," Sci. Rep. **9**(1), 6996 (2019).